PTEP

Prog. Theor. Exp. Phys. **2023** 083H01(16 pages)
DOI: 10.1093/ptep/ptad095

Performance of prototype dual gain multilayer thick gas electron multiplier with high-intensity heavy-ion beam injections in low-pressure hydrogen gas

Chihiro Iwamoto[1,*,†], Shinsuke Ota[1,2], Reiko Kojima[1], Hiroshi Tokieda[1],
Seiya Hayakawa[1], Yutaka Mizoi[3], Taku Gunji[1], Hidetoshi Yamaguchi[1],
Nobuaki Imai[1], Masanori Dozono[1], Ryo Nakajima[1], Olga Beliuskina[1],
Shin'ichiro Michimasa[1], Rin Yokoyama[1], Keita Kawata[1], Daisuke Suzuki[4],
Tadaaki Isobe[4], Juzo Zenihiro[4], Yohei Matsuda[5,6], Jun Okamoto[5],
Tetsuya Murakami[7], and Eiichi Takada[8]

[1] *Center for Nuclear Study, University of Tokyo, Wako, Saitama, Japan*
[2] *Research Center for Nuclear Physics, Osaka University, Ibaraki, Osaka, Japan*
[3] *Center for Physics and Mathematics, Institute for Liberal Arts and Sciences, Osaka Electro-Communication University, Neyagawa, Osaka, Japan*
[4] *RIKEN Nishina Center, RIKEN, Wako, Saitama, Japan*
[5] *CYRIC, Tohoku University, Aoba-ku, Sendai, Miyagi, Japan*
[6] *Department of Physics, Faculty of Science and Engineering, Konan University, Higashinada-ku, Kobe, Hyogo, Japan.*
[7] *Department of Physics, Kyoto University, Sakyo-ku, Kyoto, Japan*
[8] *National Institutes for Quantum and Radiological Science and Technology, Inage, Chiba, Japan*
[*] E-mail: chihiro.iwamoto@riken.jp
[†] Present address: Neutron Beam Technology Team, RIKEN Center for Advanced Photonics, RIKEN, Wako, Saitama, Japan

Received May 12, 2023; Revised July 6, 2023; Accepted July 11, 2023; Published July 12, 2023

A prototype Dual Gain Multilayer Thick Gas Electron Multiplier (DG-M-THGEM) with an active area of 10 cm × 10 cm was manufactured aiming at the production of a large-volume active-target time projection chamber which can work under the condition of high-intensity heavy-ion beam injections. The DG-M-THGEM has an alternating structure of electrodes and insulators. Effective gas gains of two regions, which are called beam and recoil regions, are separately controlled. Performance of the prototype DG-M-THGEM in hydrogen gas at a pressure of 40 kPa was evaluated. Irradiating a ^{132}Xe beam, an effective gas gain lower than 100 with a charge resolution of 3% was achieved in the beam region while an effective gas gain of 2000 was maintained in the recoil region. Position distributions of measured charges along the beam axis were investigated in order to evaluate gain uniformity in the high-intensity beam injection. The gain shift was estimated by simulations considering space charges in the drift region. The gain shift was suppressed within 3% even at the beam intensity of 2.5×10^6 particles per second.

Subject Index C30, H11

1. Introduction

Gaseous active targets based on time projection chambers (TPCs) [1–6] as 3D tracking detectors have been widely developed to perform experimental studies in inverse kinematics in various accelerator facilities. The gaseous active target plays an important role to measure forward-angle inelastic scattering of medium-heavy, especially unstable, nuclei in inverse kinematics. The reaction vertex can be determined by reconstructing trajectories of both beam and recoil particles simultaneously measured by the active target. Inelastic scattering measurements involving light nuclei such as proton, deuteron, and α particles at incident energies of 100–300 MeV/nucleon are well-known methods to determine the transition strength of isovector-dipole and isoscalar-monopole states [7–16]. As radioactive isotope (RI) beams of medium-heavy nuclei, such as the ^{132}Sn region, with higher intensity over 1×10^5 particles per second (pps) are becoming available at the energies for inverse-kinematics measurements of inelastic scatterings, the needs for active targets that can work under the conditions of such high-intensity beam irradiation are increasing.

Strong ionization induced by heavy-ion and high-intensity beams is discussed in Ref. [17], where the risks of sparks and malfunctioning of the detector are pointed out. The large number of ionized electrons also increase backflow ions from the multiplication part. The backflow ions distort the electric field in the drift region and reduce the accuracy of the trajectory deduction. In order to reduce these effects, the electrons and ions emerging inside an active area have to be controlled, especially along the beam trajectories. For example, the electrons and ions created by the beam particles are isolated from the drift region of MAYA [17,18] by placing plates, and that of TACTIC [19] by surrounding the beam axis with wire rings. They can accept high-intensity beams up to 5×10^7 pps, but they are not sensitive to the beam tracks. In our active target CAT-S [20], the number of the primary electrons was reduced by inserting a mesh grid in the amplification part but the gain itself was fixed [21] to get sensitivity for the beam tracks. The CAT-S with the mesh grid could detect beam trajectories, but the charge resolution was not better than 10%, which was required to achieve the aiming position resolution of 1 mm.

For improving the charge resolution of the CAT-S, we developed a Dual-Gain Thick Gas Electron Multiplier (DG-THGEM) [20]. The electrodes of the DG-THGEM at both sides are segmented to have individual gas gains for beam and recoil regions. Independent gas gains of 1×10^2 and 5×10^3 were realized for beam and recoil regions, respectively. A charge resolution better than 10% for the beam region was achieved. CAT-S with DG-THGEM could work under the condition of irradiation of RI beams including ^{132}Sn at the high intensity of 3.5×10^5 pps.

Now, we are developing a new active target TPC, named CAT-M, which has an active area of 30 cm × 30 cm, larger than CAT-S with its active area of 10 cm × 10 cm, to increase the target thickness and the acceptance for reaction events. It is necessary to employ sufficient thickness of GEMs for enlarging the active area in CAT-M, because its self-weight and Coulomb force acting between electrodes may deform itself. A Multilayer THGEM (M-THGEM) developed by Cortesi et al. [22] has an alternating structure of electrodes and insulators. This has sufficient thickness to resist deformation.

We designed a new multilayer THGEM with the capability of dual gain. We call it Dual Gain Multilayer Thick GEM (DG-M-THGEM). In the present work, the prototype DG-M-THGEM with the same active area as CAT-S of 10 cm × 10 cm was used to investigate the gain stability and charge responses with high-intensity heavy-ion beam injection. The structure of the prototype DG-M-THGEM is described in Sect. 2. The measured effective gas gain and charge resolution of the DG-M-THGEM using a heavy-ion beam and the gain shift as a function of the beam intensity are shown in Sect. 3. A summary is given in Sect. 4.

(a) Schematic drawings

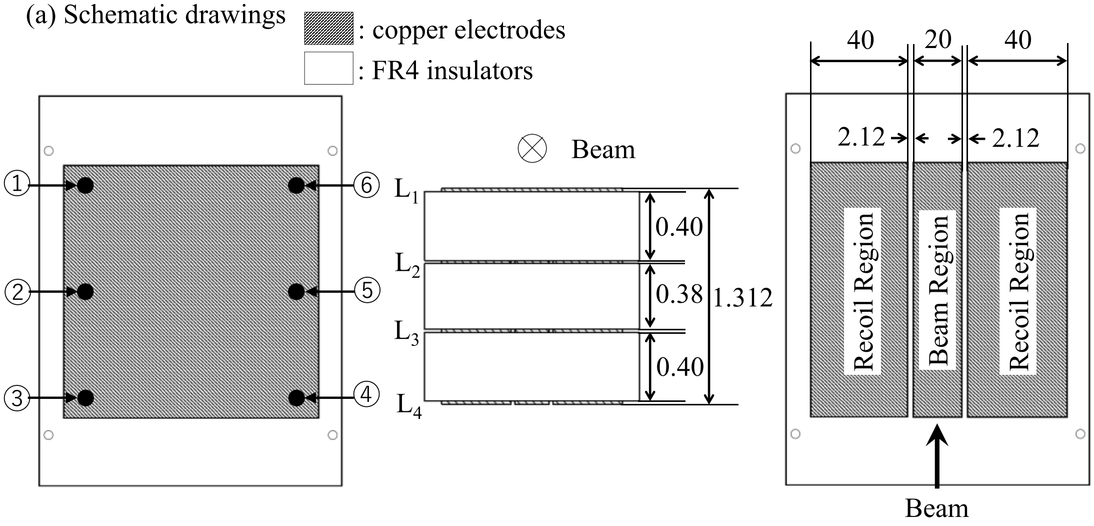

Drift region side Cross sectional view Induction region side

(b) Photographs

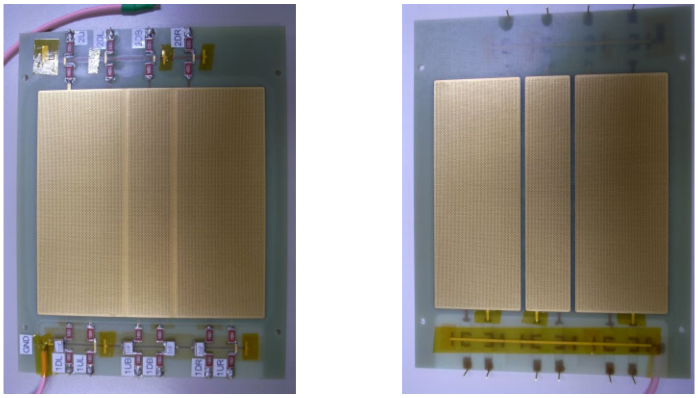

Drift region side Induction region side

Fig. 1. (a) Schematic views of prototype DG-M-THGEM. Hatched regions are copper electrodes. Plain regions are FR4 insulators. Dimensional values are in mm. Solid circles in the view from the drift region side indicate positions where the thickness of the DG-M-THGEM was measured. Each number corresponds to a measured point listed in Table 1. The four electrodes are denoted by L_1, L_2, L_3, and L_4 in the cross sectional view. Electrodes L_2, L_3, and L_4 are divided into one beam region at the center and two recoil regions at both sides as shown in the view from the induction region side. (b) Photographs of the prototype DG-M-THGEM.

2. Structure of prototype DG-M-THGEM

Figure 1 shows schematic drawings and photographs of the prototype DG-M-THGEM. It was designed by ourselves and produced by REPIC Co. Ltd, Japan. The prototype DG-M-THGEM has an alternating structure of four sheets of electrodes and three plates of insulators. Hereafter, the four electrodes are denoted by L_1, L_2, L_3, and L_4. The present production process is as follows: first, two substrates with electrode copper layers on both sides were produced, i.e. one has electrodes L_1 and L_2, and the other has electrodes L_3 and L_4. The thicknesses of the copper electrode and FR4 insulator are 0.032 mm and 0.40 mm, respectively. Then a 0.3-mm-thick FR4 plate was sandwiched by these two substrates and bonded with 0.04-mm-thick epoxy-resin glue. The actual thickness of the middle substrate is 0.38 mm including the glue thickness. And

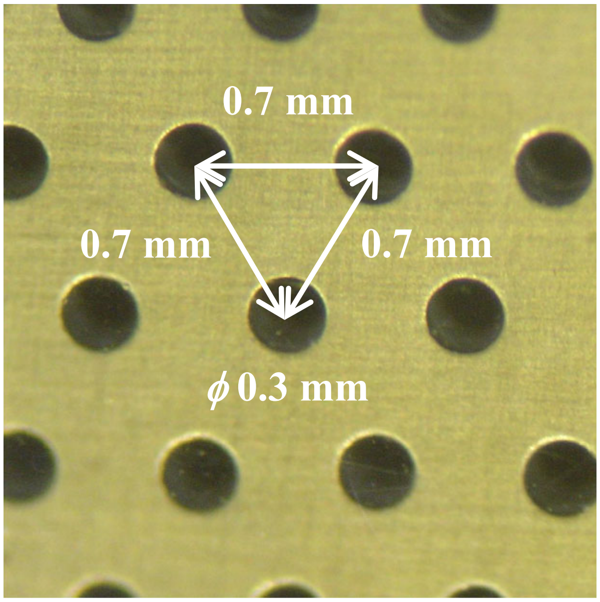

Fig. 2. Photograph of DG-M-THGEM hole array pattern. The diameter and pitch of the holes are 0.3 mm and 0.7 mm, respectively.

Table 1. Measured thicknesses of prototype DG-M-THGEM at positions indicated in Fig. 1. Each value is an average of the three measurements.

measured position	actual thickness [mm]
1	1.301 ± 0.001
2	1.290 ± 0.002
3	1.294 ± 0.002
4	1.303 ± 0.001
5	1.302 ± 0.001
6	1.297 ± 0.002

finally, GEM holes were drilled piercing from L_1 to L_4. The geometry pattern of the GEM holes is shown in Fig. 2. The diameter and the pitch of the hole are 0.3 mm and 0.7 mm, respectively. The nominal total thickness of the prototype DG-M-THGEM is 1.312 mm. The actual thickness was measured at six points which are indicated in the view of the drift region side in Fig. 1(a). Table 1 shows the thickness of each point as measured with a caliper. The value of each point is an average of three measurements. The average thickness at the six measured points is 1.298 mm and the maximum difference among the measured points is 0.002 mm. The size of the substrate is 124 mm × 160 mm, and the area of the active region is approximately 100 mm × 100 mm. Electrodes L_1 and L_4 are closest to the drift and the induction regions, respectively. Electrodes L_2, L_3, and L_4 are divided into three parts. The center one is called the "beam region", and the two side ones are called the "recoil region". The beam region is 20 mm wide to cover the envelope of the beam, and each recoil region is 40 mm wide. There are 2.12-mm width gaps between the beam and recoil regions. Electrode L_1 is not segmented in order to avoid the charge-up of the insulator. As shown in the photograph of Fig. 1(b), protective resistors and stabilization capacitors are soldered on the insulator board.

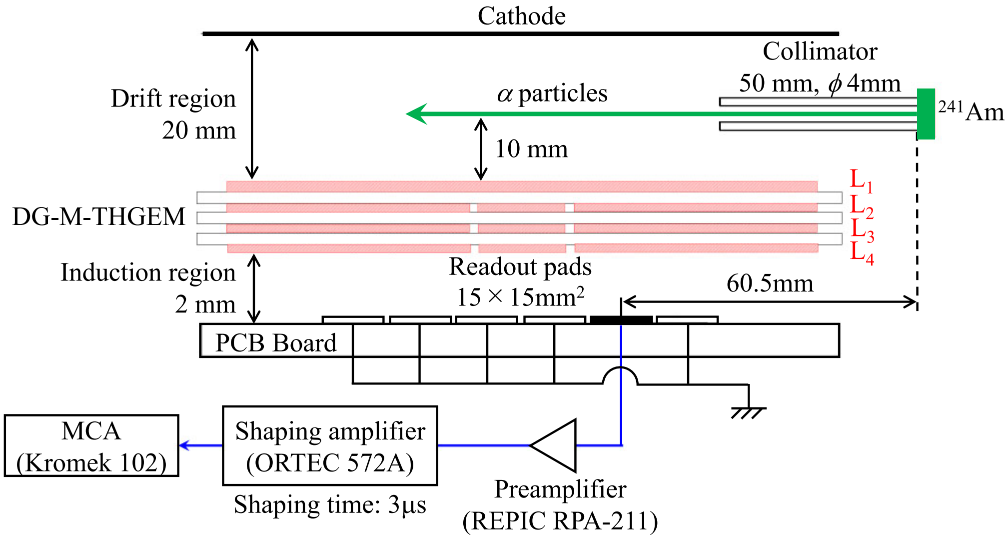

Fig. 3. Schematic view of the configuration in a test chamber and data acquisition system for effective gas gain measurement with α source ^{241}Am. Position relations of the DG-M-THGEM to the cathode, the α source, and the readout board are shown. Note that the dimensions of each component and each distance are not scaled. Rectangles on the Printed Circuit Board (PCB) are segmented electrodes. The filled rectangle indicates the readout pad whereas unfilled rectangles indicate the grounded electrodes. The readout pad was located below the recoil region of the DG-M-THGEM and the distance from the α source was 60.5 mm. Signals from the pad were measured by a multichannel analyzer after amplification by a preamplifier and shaping amplifier.

3. Performance of prototype DG-M-THGEM

For performance evaluations of the prototype DG-M-THGEM, two experiments were carried out. First, effective gas gain of the prototype DG-M-THGEM was measured with various bias settings using an α source of ^{241}Am in a test bench chamber. Second, the prototype DG-M-THGEM was installed in the CAT-S chamber. The effective-gas-gain stabilities and charge resolutions in the beam region were evaluated using a heavy-ion beam. In both case, hydrogen gas with a purity of 99.99% at a pressure of 40 kPa was filled.

3.1. *Effective gas gain evaluated using ^{241}Am α source*

A schematic view of the experimental setup to measure the effective gas gain using the ^{241}Am α source (0.98 kBq at the time of this experiment) is shown in Fig. 3. The test bench was installed in a cylindrical chamber with an inner diameter of 24 cm and a height of 12 cm. In the chamber, the hydrogen gas flowed at the rate of approximately 100 cm^3/min. The gas pressure was monitored at the inlet and the outlet position of the chamber with differential pressure gauges with an accuracy of 0.1 kPa. Oxygen concentration in the chamber was also monitored periodically at the outlet position and the oxygen concentration was kept at the 0.01% lower limit of the monitor or less. A cathode plate was placed above L_1 with a distance of 20 mm from the surface of L_1. The drift field for electrons was formed by L_1 and the cathode plate. The α particles, which were collimated by a polytetrafluoroethylene (PTFE) collimator with a length of 50 mm and an inner diameter of 4 mm, were injected to the drift field. The α particles were injected to the recoil region and passed through 10 mm above L_1. A readout board was placed 2 mm below the surface of L_4. On the readout board, 36 square-shaped copper pads, each of which has a 15 mm × 15 mm area, were arranged in 6 rows and 6 columns with

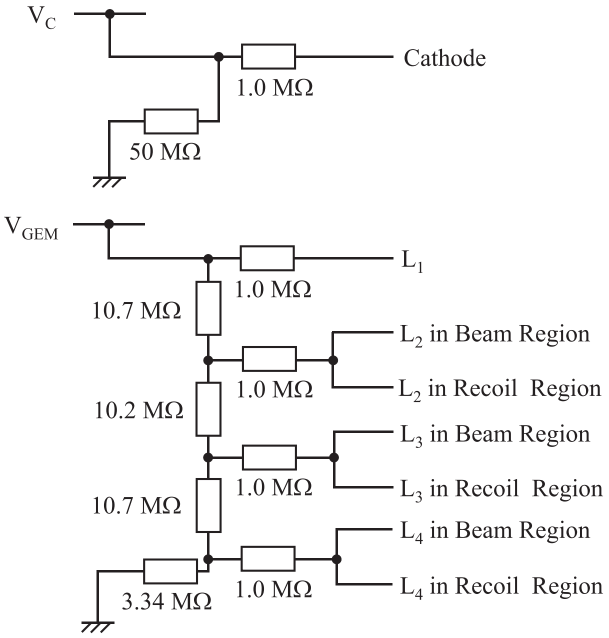

Fig. 4. Resistor configuration to supply biases to the cathode plate, and electrodes L_1, L_2, L_3, and L_4.

interval gaps of 1 mm. One pad, hereafter called the readout pad, shown as a filled rectangle in Fig. 3(a), was connected to a readout circuit. The other pads were all grounded. The distance between the center of the readout pad and the surface of the α source was 60.5 mm. The energy deposit of α particles passing through the area corresponding to the readout pad was calculated to be 115 keV by LISE++ [23]. The collected electrons on the readout pad were integrated with a charge-sensitive preamplifier, a REPIC RPA-211. Conversion gain was modified to be 400 mV/pC with a time-constant of 80 ns. The output signal from the preamplifier was pulse-shaped by a shaping amplifier, an ORTEC 572A, and its pulse height was recorded by a multichannel analyzer, a Kromek 102, a product of Kromek Group plc. In order to convert the pulse height to the absolute charge value, the circuit system was calibrated by a pulser module and charge injector (capacitance).

Figure 4 shows the resistor chain to supply biases for the cathode plate and the electrodes of the prototype DG-M-THGEM. The bias V_C is for the cathode. The bias to each electrode of the prototype DG-M-THGEM was supplied by V_{GEM} through a resistor divider. It should be noticed that the beam and recoil regions had the same bias in the present test. The field strength in the drift region, which was determined by the biases of the cathode plate and L_1, was controlled by a combination of V_C and V_{GEM} in order to keep to 1 kV/cm/atm, i.e. V_{GEM} and V_C were simultaneously changed from −1725 V to −1975 V and −2525 V to −2775 V in 25-V steps, respectively. The drift velocity of electrons is estimated to be 1 μs/cm at the present field strength by a simulation program, Garfield++ [24]. As shown in Fig. 1, the distances between L_1−L_2 and L_3−L_4 are the same, but that of L_2−L_3 is different from them; therefore, the resistor chain was adjusted so that the electric fields of L_1−L_2, L_2−L_3, and L_3−L_4 have the same strength.

The effective gas gain G_{eff} is defined as a ratio of Q_{meas} to Q_{in},

$$G_{\text{eff}} = \frac{Q_{\text{meas}}}{Q_{\text{in}}}, \tag{1}$$

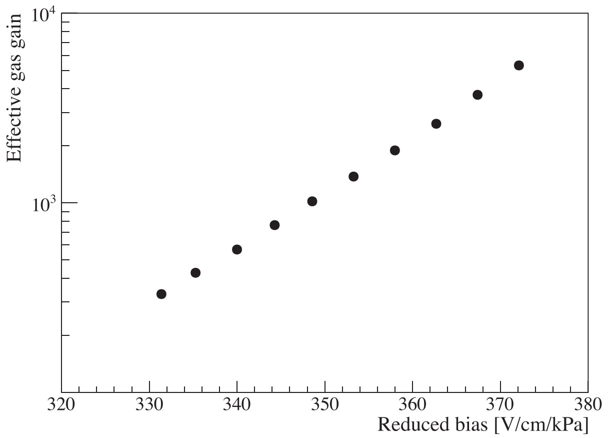

Fig. 5. Effective gas gain of prototype DG-M-THGEM as a function of reduced bias between L_1 and L_4. The reduced bias is calculated using the gas pressure monitored in each measurement.

where Q_{meas} is the measured charge from the readout pad and Q_{in} is the initial charge. Q_{in} is calculated by the elementary charge, e; stopping power of an α particle in the gas, dE/dx; mean energy for ion–electron pair creation, W; and path length of an α particle, dX. Q_{in} is described as follows:

$$Q_{\text{in}} = \frac{e}{W} \cdot \frac{dE}{dx} \cdot dX, \tag{2}$$

where we used W = 36.5 eV [25] for hydrogen gas, and $dX = 15$ mm was the length of the readout pad. The ambiguity of dX is estimated to be within 0.01 mm, because the α particles were collimated, and the angular dispersion is up to 2.3 degrees. Therefore, the dX is assumed to be same as the length of the readout pad.

Figure 5 shows the effective gas gain as a function of reduced bias. The reduced bias is derived by dividing the electric field strength between L_1 and L_4 with the distance between these electrodes of 0.12 cm and the gas pressure. The gas pressure was monitored in each measurement and it varied between 39.80 kPa and 40.19 kPa. Our required effective gas gain for the recoil region is more than 2×10^3, which was achieved with the reduced bias above 360 kV/cm/kPa. In the present condition, we could not obtain the effective gas gain over 5.31×10^3 due to discharges.

3.2. *Effective gas gain and charge resolution using heavy-ion beam*

Measurement of effective gas gain and charge resolution using a heavy-ion beam (program number 15H307) was performed at a synchrotron accelerator facility, Heavy Ion Medical Accelerator in Chiba (HIMAC), National Institutes for Quantum Science and Technology (QST). A ^{132}Xe beam with the energy of 185 MeV/nucleon from the synchrotron accelerator was introduced from the end of the beam transport line to the experimental setup and injected into the CAT-S. The repetition time of the synchrotron was 3.3 seconds. A so-called slow-extraction mode was applied to have a moderate and uniform intensity for a certain duration. The typical extraction duration was 1.5 seconds. The number of the ^{132}Xe particles in each beam pulse was monitored with a diamond detector [26] located 1077 mm upstream of the CAT-S. The position distribution of the beam was measured with two low-pressure multi-wire drift chambers (MWDCs) [27] which were installed $Z = 672$ mm and $Z = 1034$ mm downstream of the CAT-S.

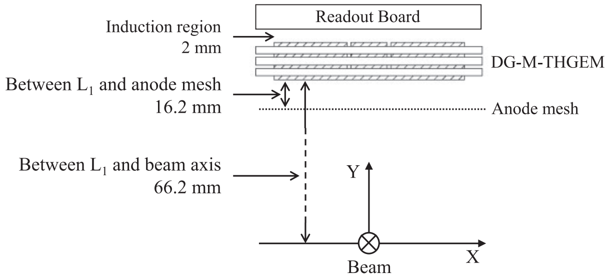

Fig. 6. Schematic view of the configuration in the CAT-S chamber for an experiment using a ^{132}Xe beam from upstream. It shows the positions of the DG-M-THGEM, anode mesh, and readout board relative to the beam axis. The origin is the center of the active area of the CAT-S on the beam trajectory.

Here we define the beam axis as Z, the horizontal axis as X, and the vertical axis as Y. Their origins are set to the center of the CAT-S active area.

The configuration of the CAT-S with the prototype DG-M-THGEM is shown in Fig. 6. It should be noticed that the configuration is upside down relative to Fig. 3. The cathode plate of the drift field is not drawn in Fig. 6. The gas pressure and flow rate were 40 kPa and 100 cm^3/min, respectively. The oxygen concentration was kept at the 0.01% lower limit of the monitor or less. The drift field formed by the CAT-S field cage was set to be 1 kV/cm/atm. Thus, the estimated drift velocity of the electron was 1 μs/cm, as was the case with the test bench experiment. The electrons drift toward the $+Y$ direction. An anode mesh was installed at 16.2 mm below L_1. The anode mesh is made of SUS304. The diameter and the pitch of the wires of the anode mesh are 30 μm and 254 μm, respectively. The electric field strength between the anode mesh and L_1 was 2.39 kV/cm/atm. The readout electrode was mounted at 2 mm above L_4. There are 416 readout pads, which have an equilateral triangle shape of 7-mm side formed on the Printed Circuit Board (PCB). The beam was injected at 66.2 mm below L_1 in the beam region. Each readout pad was connected to the preamplifier RPA-211. The output signals of the preamplifier were digitized by a V1740 flash Analog-to-Digital converter (FADC), from CAEN Co. Ltd. The sampling rate was 50 MHz. The total charge read by the pad was obtained by summing up the samples. The obtained total charge was calibrated using the pulser module and the charge injector.

Figure 7 shows the resistor configuration to supply biases to the electrodes of the prototype DG-M-THGEM. The biases to L_1 and L_2 of the recoil region were supplied by V_1 through the resistor chains. The biases to other electrodes, L_3 and L_4 of the recoil region, and L_2, L_3, L_4 of the beam region, were supplied by V_{3R}, V_{4R}, V_{2B}, V_{3B}, and V_{4B}, respectively. Consequently, the gas gain of the beam region and the recoil region can be controlled independently.

The definition of the effective gas gain is the same as Eq. (1). The Q_{in} induced by the ^{132}Xe beam was estimated similarily from the stopping power dE/dx which was calculated with LISE++ but calso onsidering the escape energy carried by delta rays. If the delta rays escape from a region of interest, the measured energy deposit becomes lower than the energy loss. The energy carried by the delta rays was estimated using GEANT4 [28]. Considering the results of both simulation and measurement, it turns out that the ratio of the escaped energy to the energy loss, ϵ_{e}, is 18.7% for the ^{132}Xe beam. In addition, charges measured by each readout pad are modified from the energy deposit due to a diffusion effect in the drift region. The ratio of the charge measured by each readout pad to the energy deposit, ϵ_{d}, was estimated by fitting the

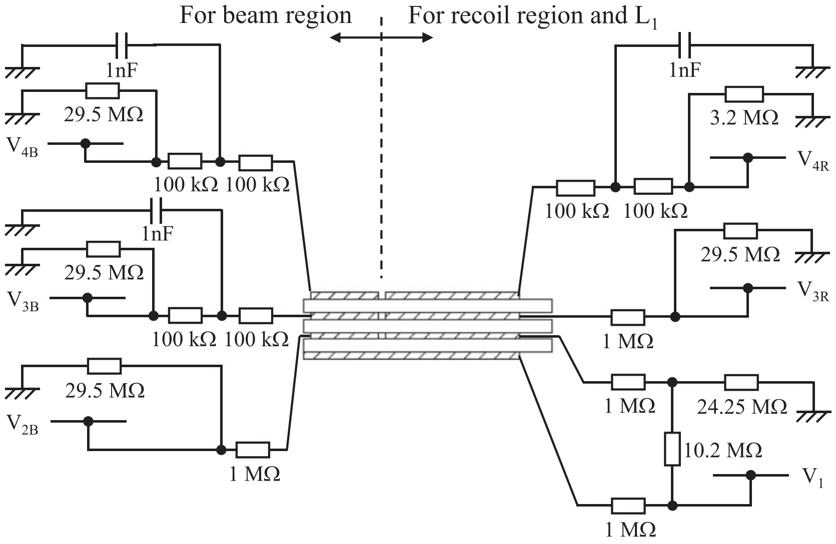

Fig. 7. Resistor configuration to supply voltage to electrodes L_1, L_2, L_3, and L_4 of the DG-M-THGEM shown in Fig. 1. The electrodes are L_1, L_2, L_3, and L_4 from the bottom of this figure. The right and left sides are for the recoil and beam regions, respectively. V_1 supplied bias to L_1 and L_2 of the recoil region with the resistor chain. As for the other electrodes, V_{3R}, V_{4R}, V_{2B}, V_{3B}, and V_{4B} supplied biases to L_3 and L_4 of the recoil region, and L_2, L_3, L_4 of the beam region, respectively.

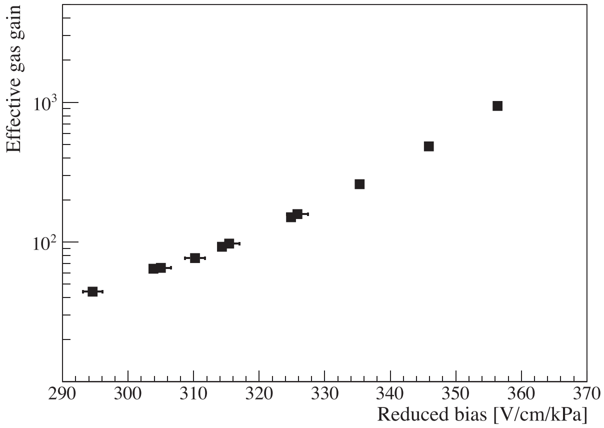

Fig. 8. Effective gas gain as a function of the reduced bias with a low-intensity ^{132}Xe beam. The reduced bias is calculated using the gas pressure monitored in each measurement.

calculated charges in the readout pads along the trajectory to the measured charges. The $Q_{\rm in}$ is modified from Eq. (2) as follows:

$$Q_{\rm in} = \frac{e}{W} \cdot \frac{dE}{dx} \cdot \epsilon_{\rm d} \cdot (1 - \epsilon_{\rm e}) \cdot dX. \tag{3}$$

Note that the ϵ_e is expected to be zero for the low-energy alpha particles. The ϵ_d is expected to be one when the readout pad has translational symmetry and the change of the stopping power is small enough compared to the energy deposit.

The effective gas gain in the beam region was measured by varying biases. Figure 8 shows the measured effective gas gain as a function of the reduced biases with the low-intensity beam of 5×10^3 particles per pulse. The effective gas gains were derived by averaging over all of the 52 readout pads in the beam region. The bias setting is summarized in Table 2. The lower bias

Table 2. Bias setting between each pair of electrodes in the beam and recoil regions for the experiment with a ^{132}Xe beam.

	beam region	recoil region
L_1-L_2	596 V	596 V
L_2-L_3	570 V	570 V
L_3-L_4	548−248 V	598 V

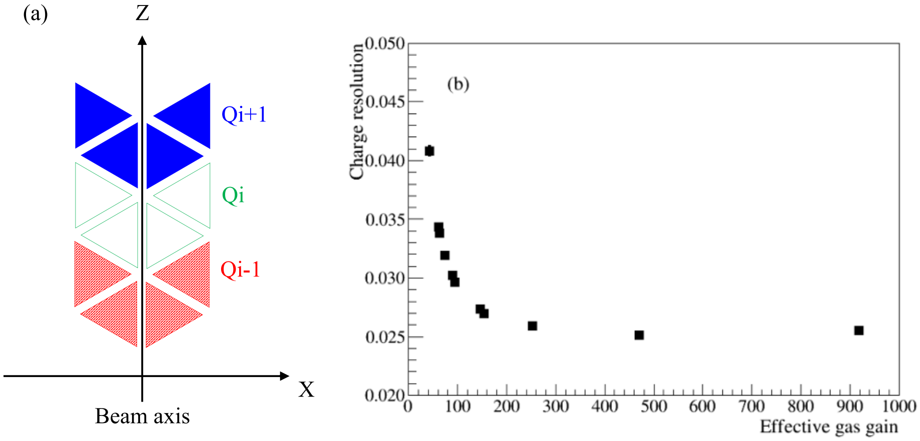

Fig. 9. (a) Definition of pad groups to evaluate charge resolutions. Four triangles with the same color are in one group. (b) Charge resolution as a function of effective gas gain.

applying to the first multiplier stage, which corresponds to between L_1 and L_2, can decrease ion backflow [22]. However, the reduction of the number of electrons at the first stage by lowering the first-stage bias is expected to cause the poor charge resolution [21]. We tried to apply slightly lower bias to the final multiplier stage of L_3–L_4 in the beam region by varying only V_{4B} while fixing V_1, V_{2B}, and V_{3B}. The biases of the recoil region, V_{3R} and V_{4R}, were fixed to make the electric fields between each electrode have the same strength. An effective gas gain lower than 1×10^2 can be achieved in the beam region while the effective gas gain of 2×10^3 at the recoil region was held. The effect of the high-intensity beam injection will be discussed in the next subsection.

Charge resolution was also derived with the same bias setting as in Table 2. In the present analysis, the charge resolution was defined as follows: pads were formed in a group defined as shown in Fig. 9(a). The neighboring four triangles are in one group. The charge collected by the i-th group is denoted by Q_i. Index, i, is ordered along the Z axis, from 0 to 12. All the Q_i is expected to be the same for all i-th groups, because the beam energy was sufficiently high and its stopping power was constant at 94.3 keV/mm within 0.2% over all the active area. Thus, we defined a residual of Q_i as follows:

$$\Delta Q = Q_i - \frac{(Q_{i-1} + Q_{i+1})}{2}. \tag{4}$$

The charge resolutions as a function of the effective gas gain are shown in Fig. 9(b). The charge resolutions were derived by averaging the 11 residual widths along the Z axis. The charge resolutions significantly depend on the effective gas gain. This indicates that the charge resolution is mainly determined by the statistics of the number of amplified electrons. A charge resolution much smaller than 10% is achieved over all the effective-gas-gain region.

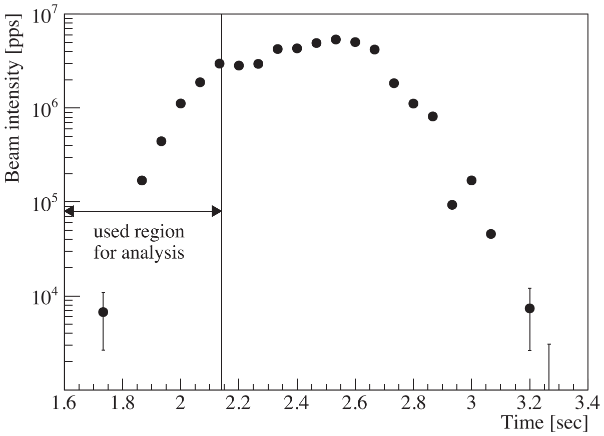

Fig. 10. Beam intensity distribution as a function of time in one beam duration when integrated intensity was 1×10^6 particles per pulse. The origin of time is arbitrary.

Table 3. Average beam intensity for each time bin used in Fig. 10.

time range [s]	average beam intensity [10^3 pps]
1.60–1.78	1.0
1.84–1.86	120
1.86–1.88	220
1.88–1.91	440
1.91–1.95	660
1.95–2.14	2500

3.3. *Test with high-intensity beam*

In this subsection, sensitivity of the effective gas gain to the beam intensity was discussed assuming the beam intensity dependence of the effective gas gain and the initial charge, as described in the following equation modified from Eq. (1):

$$Q_{\mathrm{meas}} = G_{\mathrm{eff}}(I_{\mathrm{beam}}) \times Q_{\mathrm{in}}(I_{\mathrm{beam}}). \tag{5}$$

Therefore, we consider that the Q_{in} and G_{eff} are treated as a function of the beam intensity, I_{beam}. Ideally the Q_{meas} should not be changed by I_{beam}, but it has sensitivities to I_{beam} through this equation.

The beam intensity has a time structure within the extraction duration. Figure 10 shows the beam intensity distributions within the extraction duration when the integrated intensity was 1×10^6 particles per pulse. The horizontal axis shows the time in one beam duration and the origin of the time is arbitrary. The vertical axis is the averaged beam intensity in each time bin. The maximum beam intensity is larger than the average of the total number of the beam in one duration. Considering the beam intensity derived in each time bin, we evaluated the beam intensity dependence of the effective gas gain. Table 3 shows the average beam intensity for each time bin considered in the evaluation.

Assuming that $G_{\mathrm{eff}}(I_{\mathrm{beam}})$ was not so sensitive to the beam intensity, i.e. $G_{\mathrm{eff}}(I_{\mathrm{beam}}) = G_{\mathrm{nom}}$, we derive $Q_{\text{in-m}}(I_{\mathrm{beam}}) = Q_{\mathrm{meas}}/G_{\mathrm{nom}}$ as shown in Fig. 11. Here we presumed the nominal effective gas gain, $G_{\mathrm{nom}} = 76.7$, was the effective gas gain obtained in the low-intensity ^{132}Xe beam experiment at the supplied bias of 323 V between L_3 and L_4 in the beam region. Figure 11

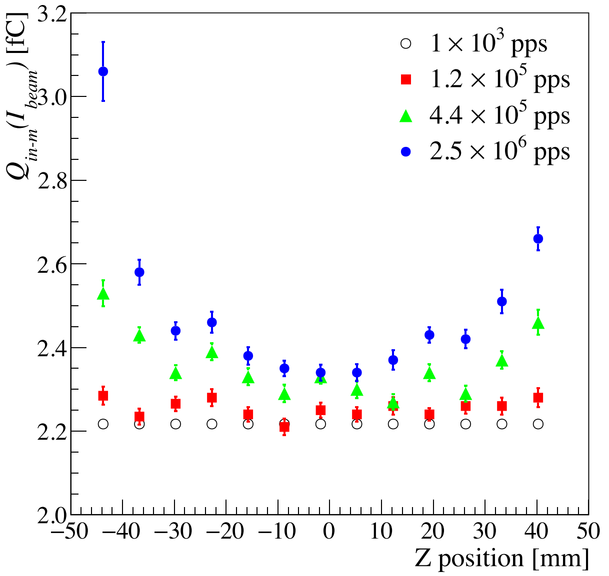

Fig. 11. $Q_{\text{in-m}}(I_{\text{beam}})$ distribution as a function of Z, where $Q_{\text{in-m}}(I_{\text{beam}})$ depends on beam intensity also.

shows $Q_{\text{in-m}}(I_{\text{beam}})$ depends not only on the beam intensity but also on the position along the beam axis (Z). As the beam intensity increases, $Q_{\text{in-m}}(I_{\text{beam}})$ increases overall Z. The distribution has a parabolic shape with a symmetry at $Z = 0$.

To explain this parabolic shape, we employed the "ion pillar model" [29]. The ion pillar model has been proposed to evaluate electric field distortion in the drift region caused by the ion-backflow from GEMs. The backflow ions move from the GEMs to the cathode, then a pillar of positive ions along the beam trajectory is formed. In previous studies, electric field distortion in the drift direction (Y direction) has been discussed, but similar electric field distortion also occurs along the beam axis (Z direction) and its vertical direction (X direction). The ions attract drifting electrons from outside the beam region, consequently $Q_{\text{in-m}}(I_{\text{beam}})$ increases in the beam region. The number of ions increases with increments of the beam intensity, hence the behavior of $Q_{\text{in-m}}(I_{\text{beam}})$ in Fig. 11 can be explained. Figure 12 shows the comparison of the beam profile on the X axis as measured by the CAT-S and the MWDCs. The beam profile measured by the MWDCs shows a similar size independent of the beam intensity. However, the one measured by the CAT-S was observed to become narrow according to the beam intensity, because the attracted electrons converge on the beam axis.

The effect of ions in the pillar on electrons which reach to L_1 was investigated by electron-drift simulation. The ion density in the pillar was assumed to be distributed homogeneously in the Z and Y directions and Gaussian in the X direction. The width of the ion pillar in the X direction was the beam width measured with the CAT-S as shown in Fig. 12 because the number of ions in the pillar is due to the backflow ions that the attracted drifting electrons generate in the DG-M-THGEM. The beam was injected 5 cm below L_1. The distance from L_1 to the cathode plane of the field cage was approximately 250 mm. The drift velocities of a hydrogen ion and an electron were 0.01 cm/μs and 1.2 cm/μs, respectively. Thus, the time for the backflow ions to reach the cathode was approximately 3 ms. As shown in Table 3, the time bin for each beam intensity was from about 20 ms to 200 ms. Therefore, the number of the ions in the pillar was considered to be immediately saturated depending on the beam intensity within the time bin.

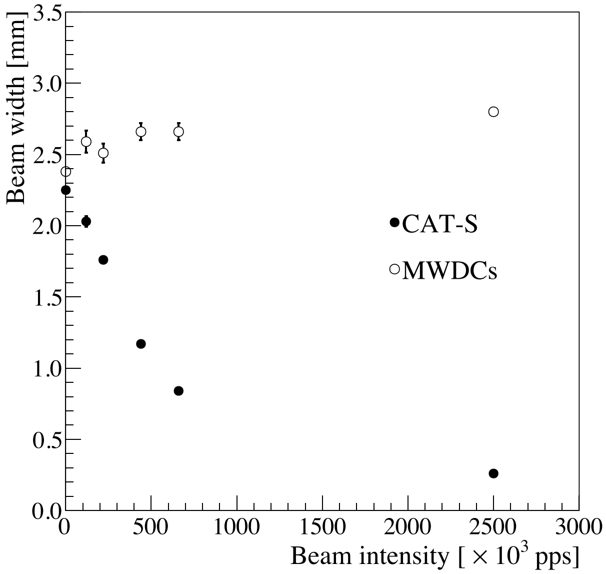

Fig. 12. Beam profile on *X* axis derived by the CAT-S and MWDCs. The beam width measured by the CAT-S shrank due to the effect of the ion pillar with beam intensity increments, whereas no effect is shown by the MWDCs.

The number of the electrons reaching to L_1 along the beam trajectory, $Q_{\text{in-s}}(I_{\text{beam}})$, was derived by the electron-drift simulation with Garfield++ [24] while varying the amount of ions in the pillar.

To reproduce $Q_{\text{in-m}}(I_{\text{beam}})$ in Fig. 11, we explain $Q_{\text{in-m}}(I_{\text{beam}})$ using $Q_{\text{in-s}}(I_{\text{beam}})$ as follows:

$$Q_{\text{in}-\text{m}}(I_{\text{beam}}) = \frac{Q_{\text{meas}}}{G_{\text{nom}}} = \frac{Q_{\text{in}-\text{s}}(I_{\text{beam}}) \times G_{\text{eff}}(I_{\text{beam}})}{G_{\text{nom}}}. \tag{6}$$

We set $Q_{\text{in-s}}(I_{\text{beam}})$ and $G_{\text{eff}}(I_{\text{beam}})$ as the fitting parameters in the least-square fitting method to reproduce the $Q_{\text{in-m}}(I_{\text{beam}})$ in Fig. 11. Because $Q_{\text{in-s}}(I_{\text{beam}})$ is dependent on the amount of ions in the pillar, the actual parameters to be varied are the amount of ions in the pillar and the effective gas gain. Figure 13(c) and (d) shows the fitting results of the distributions of the χ^2 as a function of the amount of ions in the pillar and effective-gas-gain shift for the beam intensities of 1.2×10^5 and 2.5×10^6 pps, respectively. Here, the effective-gas-gain shift is defined as $\{G_{\text{eff}}(I_{\text{beam}}) - G_{\text{nom}}\}/G_{\text{nom}}$. Searching for the χ^2 minimum point in Fig. 13(c), the number of ions in the pillar and the effective-gas-gain shift are 2.6×10^2 pC and -1%, respectively. Using these parameters, we can reproduce the $Q_{\text{in-m}}(I_{\text{beam}})$ spectrum as shown in Fig. 13(a). Figure 13(b) is also reproduced by 1.38×10^3 pC and and 0.4%. This result shows that the ion backflow from the DG-M-THGEM is significantly large to show its effect. The required effective gas gain in the beam region was achieved with the dual gain operation by the lower bias application between L_3 and L_4 in the beam region; however, the ion backflow effect was not sufficiently small.

Figure 14 shows the beam intensity dependence of the amount of ions in the pillar and the effective-gas-gain shift. Comparing the beam intensity of 2.5×10^6 pps with 1.2×10^5, the gain fluctuation is suppressed within 3% while the amount of ions increases by seven times. It was found that the amount of ions in the pillar was saturated above the beam intensity of 6×10^5 pps. It is considered to be due to decreasing the ion backflow from the DG-M-THGEM as the amount of ions in the pillar increases above a certain level, similar to the trend shown in a

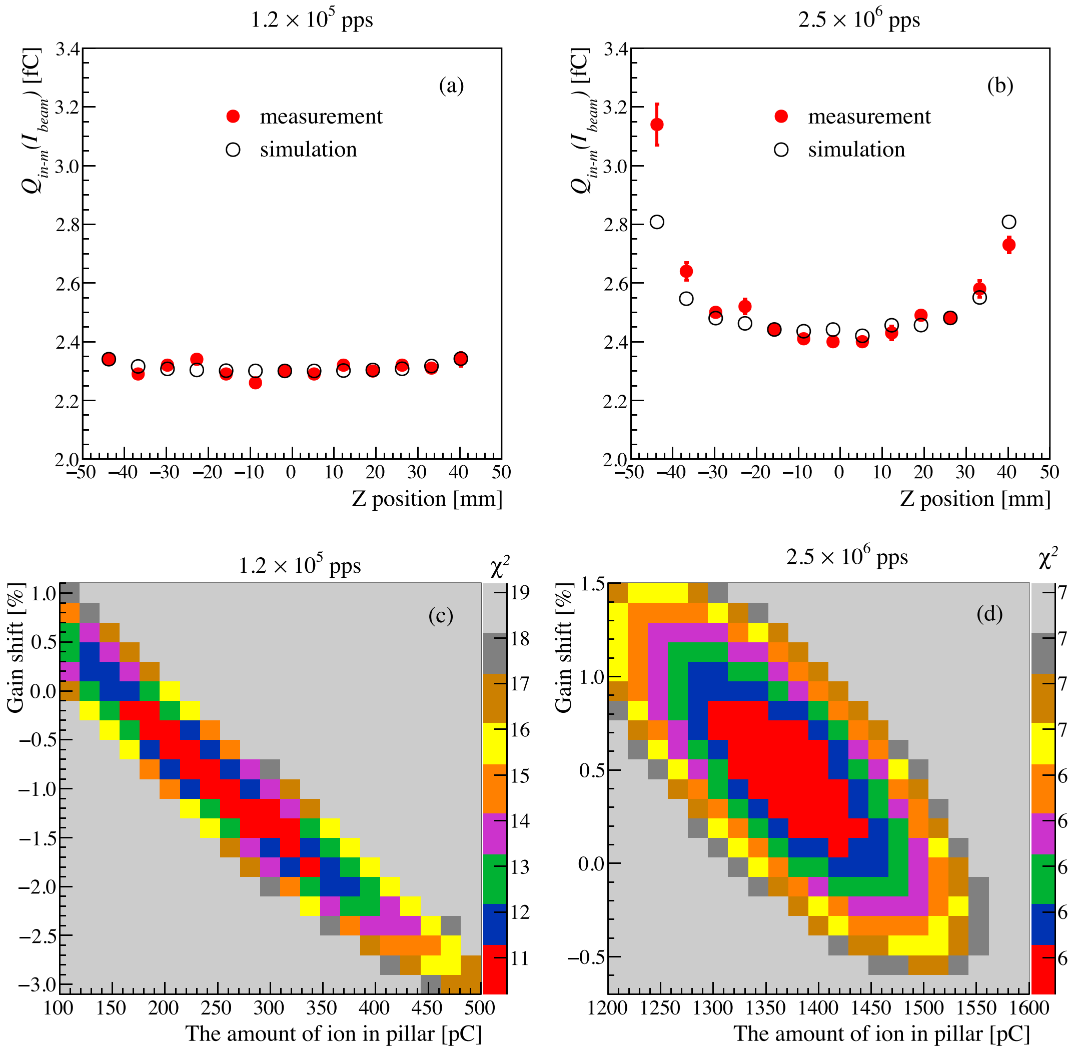

Fig. 13. (a) and (b) Position distributions of $Q_{\text{in-m}}(I_{\text{beam}})$, which is the number of electrons reaching electrode L_1 of DG-M-THGEM, along the beam trajectory Z at the beam intensities of 1.2×10^5 and 2.5×10^6 pps, respectively. Solid circles and open circles are measured values and simulated results at the χ^2 minimum by the least-square fitting, respectively. (c) and (d) χ^2 distributions as a function of the amount of ions in the pillar and effective-gas-gain shift at the beam intensities of 1.2×10^5 and 2.5×10^6 pps, respectively.

previous study [30]. The fluctuation of the effective gas gain was sufficiently suppressed to the same level as the charge resolution at the effective gas gain of 1×10^2. As shown in Fig. 12, the electrons were attracted by the ion pillar to the beam center; therefore, the electron density increased by a factor of 8.5 at 2.5×10^6 pps compared to at 1×10^3 pps beam intensity. It can be concluded that the gain fluctuations were suppressed to 3% even under conditions where ionized electrons of 6 pC/cm²/s flow to the prototype DG-M-THGEM.

4. Summary

The prototype DG-M-THGEM with an active area of 10 cm × 10 cm was produced and its performance was evaluated. The electrodes of the multilayer-thick GEM, which has an alternating structure of electrodes and insulators, were segmented into three regions. The center

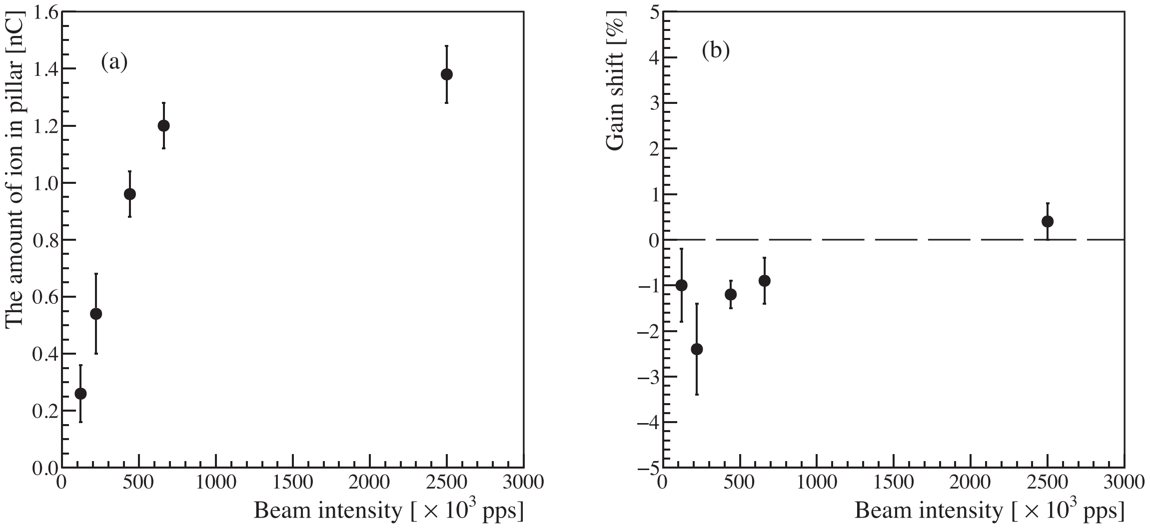

Fig. 14. (a) The amount of ions in the pillar as a function of beam intensity. (b) Effective-gas-gain shift as a function of beam intensity.

region and both sides can have biases applied independently to control gas gains individually. The performance of the prototype DG-M-THGEM was evaluated using hydrogen gas at the pressure of 40 kPa. The effective gas gains as a function of the reduced bias applied to DG-M-THGEM were measured using the α source of ^{241}Am. The effective gas gain was achieved up to 5.31×10^3.

The effective gas gain and the charge resolutions in the beam region were evaluated using the heavy-ion ^{132}Xe beam with the energy of 185 MeV/nucleon and intensity from 5×10^3 to 1×10^6 particles per pulse. An effective gas gain of lower than 1×10^2 was achieved with a charge resolution of smaller than 3% in the beam region while maintaining the effective gas gain of 2×10^3 in the recoil region. The effective-gas-gain stability of the low-gain beam region when increasing the beam intensity was also discussed. As the beam intensity increases, the initial charges become larger, because the ion pillar attracts electrons. The effect shrank the beam width measured by the CAT-S as the beam intensity increased. Even if increasing the beam intensity from 1.2×10^5 pps to 2.5×10^6 pps, the effective gas gain fluctuated within only 3% while the amount of ions increased by seven times. The effective-gas-gain fluctuation was suppressed to the same level as the charge resolution at the effective gas gain of 1×10^2. The number of electrons around the beam center was about 8.5 times larger at 2.5×10^6 pps than at 1×10^3 pps due to the effect of electrons being attracted by the ions in the pillar. The effective gas gain fluctuates within 3% even under conditions where ionized electrons of 6 pC/cm^2/s flow to the prototype DG-M-THGEM. As a future issue, it is necessary to develop a way to reduce the effect of the ion backflow in order to perform accurate tracking analysis of the trajectory.

Acknowledgements

This work was performed in part as the Research Project with Heavy Ions at NIRS-HIMAC (program number 15H307). The present work was supported by Japan Society for the Promotion of Science KAKENHI, Grant Numbers JP23740174, JP15H00834, JP16H06003.

References

1 C. E. Demonchy et al., Nucl. Instrum. Methods Phys. Res. Sect. A **583**, 341 (2007).
2 D. Suzuki et al., Nucl. Instrum. Methods Phys. Res. Sect. A **691**, 39 (2012).
3 T. Roger et al., Nucl. Instrum. Methods Phys. Res. Sect. A **895**, 126 (2018).
4 Y. Mizoi et al., Nucl. Instrum. Methods Phys. Res. Sect. A **431**, 112 (1999).
5 T. Hashimoto et al., Nucl. Instrum. Methods Phys. Res. Sect. A **556**, 339 (2006).
6 T. Furuno et al., Nucl. Instrum. Methods Phys. Res. Sect. A **908**, 215 (2018).
7 A. Tamii et al., Phys. Rev. Lett. **107**, 062502 (2011).
8 T. Hashimoto et al., Phys. Rev. C **92**, 031305(R) (2015).
9 S. Bassauer et al., Phys. Rev. Lett. **102**, 034327 (2020).
10 C. Iwamoto et al., Phys. Rev. Lett. **108**, 262501 (2012).
11 D. Patel et al., Phys. Lett. B **735**, 387 (2014).
12 D. Patel et al., Phys. Lett. B **726**, 178 (2013).
13 M. Uchida et al., Phys. Lett. B **557**, 12 (2003).
14 M. Itoh et al., Phys. Rev. C **68**, 064602 (2003).
15 K. B. Howard et al., Phys. Lett. B **807**, 135608 (2020).
16 T. Li et al., Phys. Rev. Lett. **99**, 162503 (2007).
17 C. Rodríguez-Tajes et al., Nucl. Instrum. Methods Phys. Res. Sect. A **768**, 179 (2014).
18 J. Pancin , J. Gibelin, M. Goth, P. Gangnant, J-F. Libin, R. Raabe, T. Roger, and P. Roussel-Chomaz, JINST **7**, P01006 (2012).
19 S. P. Fox et al., J. Phys. Conf. Ser. **312**, 052007 (2011).
20 S. Ota , H. Tokieda, C. S., and Y. N. Watanabe, J. Radioanal. Nucl. Chem. **305**, 907 (2015).
21 S. Ota et al., JPS Conf. Proc. **6**, 030117 (2015).
22 M. Cortesi, S. Rost, W. Mittig, Y. Ayyad-Limonge, D. Bazin, J. Yurkon, and A. Stolz, Rev. Sci. Instrum. **88**, 013303 (2017).
23 O. Tarasov and D. Bazin, Nucl. Instrum. Methods Phys. Res. Sect. B **266**, 4657 (2008).
24 R. Veenhof, Nucl. Instrum. Methods Phys. Res. Sect. A **419**, 726 (1998) .
25 C. Simon Wedlund, G. Gronoff, J. Lilensten, H. Ménager, and M. Barthélemy, Ann. Geophys., **29**, 187 (2011).
26 S. Michimasa et al., Nucl. Instrum. Methods Phys. Res. Sect. B **317**, 710 (2013).
27 H. Miya et al., Nucl. Instrum. Methods Phys. Res. Sect. B **317**, 701 (2013).
28 S. Agostinelli et al., Nucl. Instrum. Methods Phys. Res. Sect. A **506**, 250 (2003).
29 H. Ishiyama et al., JINST **7**, C03036 (2012).
30 M. Ball , K Eckstein, and T Gunji, JINST **9**, C04025 (2014).